

Energy Advances

Accepted Manuscript

This article can be cited before page numbers have been issued, to do this please use: L. M. Murillo Herrera, C. J. Mingoés, J. M. Obrero-Pérez, J. R. R. Sanchez-Valencia, M. W. Thielke, A. Barranco and A. B. Jorge, *Energy Adv.*, 2024, DOI: 10.1039/D4YA00383G.



This is an Accepted Manuscript, which has been through the Royal Society of Chemistry peer review process and has been accepted for publication.

Accepted Manuscripts are published online shortly after acceptance, before technical editing, formatting and proof reading. Using this free service, authors can make their results available to the community, in citable form, before we publish the edited article. We will replace this Accepted Manuscript with the edited and formatted Advance Article as soon as it is available.

You can find more information about Accepted Manuscripts in the [Information for Authors](#).

Please note that technical editing may introduce minor changes to the text and/or graphics, which may alter content. The journal's standard [Terms & Conditions](#) and the [Ethical guidelines](#) still apply. In no event shall the Royal Society of Chemistry be held responsible for any errors or omissions in this Accepted Manuscript or any consequences arising from the use of any information it contains.

Analysis of the Impact of Remote Oxygen Plasma Treatment on the Surface Chemistry and Electrochemical Properties of Graphite Felt Electrodes for Redox Flow Batteries

View Article Online
DOI: 10.1039/D4TA00383G

L. Mauricio Murillo-Herrera^{[a]*}, Carlos J. Mingoos^[a], J. Obrero-Pérez^[b], Juan R. Sánchez-Valencia^[b], Michael W. Thielke^[a], Ángel Barranco^[b], Ana B. Jorge Sobrido^{[a]*}.

^[a]School of Engineering and Materials Science. Queen Mary University of London. Mile End Rd, London E1 4NS, United Kingdom

^[b]Instituto de Ciencia de Materiales de Sevilla. Consejo Superior de Investigaciones Científicas. c/Américo Vespucio 49, 41092, Sevilla, Spain.

Abstract

The effects of a remote oxygen plasma (ROP) treatment on the surface of commercial graphite felts were investigated and compared against a conventional thermal treatment. In contrast to methodologies where the sample is directly exposed to the plasma, ROP allows for a high control of sample-plasma interaction, thereby avoiding extensive etching processes on the fibre surface. The impact of ROP treatment time, the electrodes were subjected to three different periods (10, 60, 600 seconds). X-ray photoelectron spectroscopy showed that the ROP treatment introduced nearly three times more surface oxygen functionalities than the thermal treatment. Raman spectroscopy measurements revealed significant increase in amorphous carbon domains for the ROP samples. The thermal treatment favoured increases in graphitic defects and resulted in an order of magnitude larger ECSA compared to the ROP treated materials despite having lower content in oxygen functionalities. The electrochemical analysis showed enhanced charge-transfer overpotentials for the GF400. The ROP samples exhibited lower mass-transport overpotential than the thermally treated material and similar permeabilities, which overall translated to the thermal treatment offering better performance at fast flow rates. However, at slow flow rates ($\sim 10 \text{ mL min}^{-1}$) the ROP treatment for the shortest period offered comparable performance to conventional thermal treatment.

Introduction

To reduce the dependence on fossil fuels and be able to rely on naturally intermittent renewable energies such as solar and wind, large-scale efficient energy storage technologies must further be developed at lower costs. This is essential to ensure a stable electrical grid supply to meet demand at any given time. Redox flow batteries (RFBs) are one of the most promising large-scale energy storage technologies to support intermittent power generation. One of the unique aspects of RFBs is their ability to decouple power and energy, which enables increasing energy capacity by increasing the volume and concentration of the electrolytes, while power output can be scaled by expanding the stack size.

A key component of RFBs is the electrodes, whose role is to enable the electrochemical reaction between the half cells. RFB electrodes need to be able to withstand the pressure arising from the flow of electrolytes, while providing a high electrochemically active surface area to promote performance, durability, and lifetime of the battery.

Graphite felts (GF) are popular materials as electrodes for these batteries due to their commercial availability, high conductivity, large surface area, while still being at a relatively low price.³ Nevertheless, pristine GF exhibits poor wettability and electrochemical activity for most redox reactions in aqueous electrolytes, due to lack of reactive sites and hydrophobic



surface. This translates into large overpotentials, low efficiencies and reaction rates.^{4, 5} Different approaches have been reported to overcome these drawbacks, primarily focused on the chemical modification of the surface. One strategy involves the introduction of heteroatom functionalities such as nitrogen⁶ or phosphorus,^{7, 8} which promote the interaction with the electroactive species through built-in defects at the fibre surface. Other strategies involve the immobilisation of transition metal nanoparticles^{9, 10}, carbon nanoparticles¹¹, and the deposition of biomass-derived carbon particles¹² onto the surface area of the GF. The poor wettability of the GF electrodes has also been enhanced through thermal treatment^{5, 13-16}, chemical modification¹⁷⁻¹⁹ or oxygen and air plasma treatments.²⁰⁻²²

Direct exposure to oxygen plasma has been reported to modify the surface of the GF, increasing roughness, leading to increases of the electrochemical active surface area and the addition of oxygen-containing functional groups (phenolic, quinone, epoxy or carboxylic acids), increasing the number of electrochemically active sites.²⁰⁻²² The use of reactive ROP treatments allows for high degree of control of the interaction between the plasma and the sample, avoiding extensive etching processes, which are characteristic of protocols involving direct exposure to oxidative plasmas.²³

In this report, we examined the effects a ROP treatment on the surface of commercial GF. The felts were exposed to the plasma for three different periods (10, 60, 600 seconds per side) to determine the influence of the plasma treatment exposure on the surface properties. The ROP-treated materials were compared against a commonly employed thermal treatment method.⁵ Electrochemical and hydraulic experiments in a single-electrolyte flow cell were carried out to establish correlations between surface properties and flow cell performance. Our results showed that all plasma-treated samples developed larger surface oxygen populations than the thermal treated sample and different surface features. However, the electrochemical performance was not directly correlated with the amount of oxygen. Instead, an interplay between surface area, oxygen functionalities and graphite defects were responsible for the enhancements observed in the flow cell performance.

Experimental

Remote plasma treatments for the preparation of modified electrodes: GF samples were positioned within a remote Electron Cyclotron Resonance Microwave (ECR-MW) plasma reactor operating at 2.45 GHz with a power of 350 W. A complete description of the experimental set-up can be found elsewhere.²³ The samples were placed at 6 cm from the glow discharge region. Before the plasma treatment, the system was evacuated to attain a base pressure of 10^{-6} mbar. Then, an oxygen flow was dosed with a calibrated mass flow controller set at 6 sccm. The gas pressure was controlled via an automated butterfly valve regulator, which controls the pumping flow of the system to maintain the pressure at 10^{-3} mbar. Three independent batches of graphite felt samples underwent O_2 plasma conditions in three different periods: 10 seconds, 60 seconds, and 600 seconds. To ensure a uniform plasma treatment of the GF, both sides of the samples were exposed to the plasma for the specified duration on one side and then flipped and treated for the same duration on the other. The substrates remained at room temperature during the treatments, as determined by a thermocouple in the sample holder.

Preparation of modified electrodes using the thermal treatment. A piece of GF of 3.18 mm thickness (ThermoFisher Scientific) was placed inside a ceramic crucible and baked at 400 °C for 30 h using a Carbolite Gero box furnace and a heating ramp of 10 °C min⁻¹.

Electrolyte preparation: The 50% SoC iron electrolyte consisted of a 0.25 M solution of iron (II) chloride tetrahydrate 98% (Sigma Aldrich UK) and iron (III) chloride hexahydrate 97%



(Sigma Aldrich UK) in 2 M hydrochloride acid (Fisher scientific UK) for an overall 0.5 M iron concentration. The supporting electrolyte for the ECSA measurements consisted of 2.6 M sulfuric acid (ChemLab Belgium).

Surface characterization: Field emission scanning electron microscopy (SEM, FEI, Inspect F50) was used to analyse the morphology of the graphite felt surfaces. X-ray photoelectron spectroscopy (XPS, Thermo Scientific, Nexsa) was used to study the chemical composition of the fibres surface. Survey scans parameters: 50 eV pass energy, 10 scans, 50 s dwell time. C 1s, O 1s, high resolution spectrum parameters: 50 eV pass energy, 30 scans, 50 s dwell time. A set of asymmetric convoluted Gaussian and Lorentzian curves was used to model the C=C contribution to the high resolution C1s spectrum. For the rest of the contributions, symmetric Gaussian and Lorentzian convoluted line shapes were used. BET analysis was performed in a Nova Quantachrome instrument, using N₂ as adsorbate. Raman spectroscopy was performed using a Renishaw in Via instrument, equipped with a 660 nm laser. The spectra were obtained by performing 10 acquisitions with 30 s of exposure between 850 and 3300 cm⁻¹ using an x20 objective lens. The Raman spectra were acquired using 5% of the laser power to avoid etching effects from biasing the I_D/I_G ratio of the fibres.

Single-electrolyte cell setup: The single-electrolyte cell active area size was 5.0625 cm². The setup consisted of a couple of PAN-based graphite felt electrodes (ThermoFisher Scientific) with a thickness of 3.18 mm separated by Nafion 115 membrane (previously soaked in 2 M sulfuric acid for several days). The electrodes and membrane were compressed by PTFE gaskets of 2.132 mm thickness (33% compression). The flow fields consisted of two graphite plates with single inlet and outlet and six interdigitated channels with a 2.1 cm channel length and 0.1 cm channel width. The rest of the device consisted of copper current collectors, stainless-steel plates and PTFE tubes with an inner diameter of 3/16 inches. In a single-electrolyte setup, the cell is connected in such a way that the same electrolyte flows through both cathode and anode.^{24, 25} A single-electrolyte cell schematic can be found in Fig. S22 in the SI document. A dual channel Walston Marlow 323 series peristaltic pump (Fisher Scientific UK) and rubber tubes connected to the PTFE tubes using push-in fittings was used to distribute electrolyte through the system. Before each experiment a calibration curve for the pump was developed by recording five sets of volume and flow periods at different pump speeds.

Single-electrolyte cell impedance: The potentiostatic impedance data was acquired using a Biologic SP300 potentiostat at the cell open circuit potential and a potential sinus amplitude of 10 mV within a range of 1 MHz to 0.1 Hz and 8 points per decade. To fit the impedance spectra, a modified Randles equivalent circuit was used. It was composed of an inductor connected in series to a resistor representing the cell internal resistance (R_s), connected in series to a parallel circuit featuring a CPE element to describe the double layer capacitance of the electrode (CPE_{dl}), and a resistor modelling charge-transfer contributions (R_{ct}) in series to a Warburg short element (W_d) to describe mass-transfer impedance in porous electrodes.²⁵ A schematic of the equivalent circuit is shown in Figure 3. All experiments were done by triplicate, for convenience only the third Nyquist plot is represented.

Single-electrolyte cell polarisation: The polarisation plots were obtained a Gamry E5000 series potentiostat. The experiment consisted of 24 chronoamperometric steps within a range of 25 mV to 600 mV. The timeframe of every chronoamperometric step was 30 s and the current data collection was done every second, from which the last 10 current values were averaged and used to build the polarisation plot. Before every set of 24 chronoamperometries, a high frequency impedance measurement was obtained to estimate the ohmic resistance of



the cell to perform an ohmic-drop correction of the potential values. All the polarisation experiments were done by triplicate.

Single-electrolyte cell Electrochemical active surface area determination: The electrochemical double layer capacitance of the materials was obtained by cyclic voltammetry experiments in 2.6 M sulfuric acid at five different scan rates: experiments at 10, 20, 40, 80 and 160 mV s⁻¹. A 400 mV potential window between -200 mV and 200 mV was used to avoid any Faradaic processes and ensuring that all the current was due to the electrode's double layer capacitance. The absolute value of the currents corresponding to the middle region of the voltammograms were averaged and plotted against the scan rate to obtain the double layer capacitance according to equation 1. To derive the qualitative ECSA, the relationship in equation 2 was used, where C_s is 23 μF cm⁻², the specific capacitance value of glassy carbon in 4 M sulfuric acid.²⁶

$$I = C \frac{dE}{dt} \quad (1)$$

$$C_s = \frac{C}{\text{Area}} \quad (2)$$

Pressure drop determination: The flow cell was rearranged to only distribute fluid through one of the sides. For this measurement, the membrane was replaced with a layer of plastic and aluminium foil and the acidic aqueous electrolyte by ultrapure water. A couple of Fluke 700RG29 digital pressure gauges (RS components UK) were installed in the cell inlet and outlet to record the pressure difference. A schematic of a flow cell modified to perform pressure drop experiments can be found in *Fig. S18* in the SI document. To obtain the permeability of the electrodes, the experimental pressure drop data was fitted using the Darcy-Forchheimer model displayed in equation 3, where Δ*P* is the pressure drop in Pa, *x* is the characteristic path length, in this case the electrode length in m, μ is the fluid dynamic viscosity in Pa s, κ is the permeability in m², ρ is the fluid density in Kg m³, β is the Forchheimer coefficient in m⁻¹ and *v* is the fluid linear velocity in m s⁻¹.²⁵

$$\frac{\Delta P}{x} = \frac{\mu}{\kappa} v + \beta \rho v^2 \quad (3)$$

The fluid linear velocity was calculated considering an interdigitated flow field according to equation 4, *Q* is the flow rate in cm³ s, *N_i* a dimensionless quantity corresponding to the number of interdigitated channels, *h_c* is the thickness of the compressed electrode in cm, and *l_c* is the length of the interdigitated channels.²⁷

$$v = \frac{Q}{N_i h_c l_c} \quad (4)$$

Results

Surface characterisation.

The chemical composition of the surface of the various electrodes was characterised using XPS. The atomic percentages of oxygen in the pristine felt **GF**, thermally treated felt **GF400**, and plasma treated felts, **P10s**, **P60s** and **P600s** were found to be 2.15% ± 0.45%, 4.14% ± 0.54%, 13.58% ± 0.24%, 10.42% ± 0.33% and 10.87% ± 0.78%, respectively. Both thermal and ROP treatments introduced oxygen on the surface of the carbon materials. All the plasma treatments resulted in higher amounts of oxygen functionalities compared to the thermal treatment, in agreement with previous research on the modification of graphite felt electrodes.^{5, 13, 20, 21, 28} This is relevant in the context of VRFBs, since previous research had identified oxygen functional groups such as C-O and O-C=O as active or catalytic sites for



outer-shell vanadium electrochemical reactions.^{5, 8, 15, 20, 28-30} However, there is still an open debate in relation to the role of the oxygen functionalities, whether these act as catalytic sites, improve wettability of the electrodes, or both.^{14, 15} The thermal and plasma treatments also introduced graphite defects and increase the surface area of the carbons, all of which can also contribute to the enhancement in performance.^{4, 14, 16, 28}

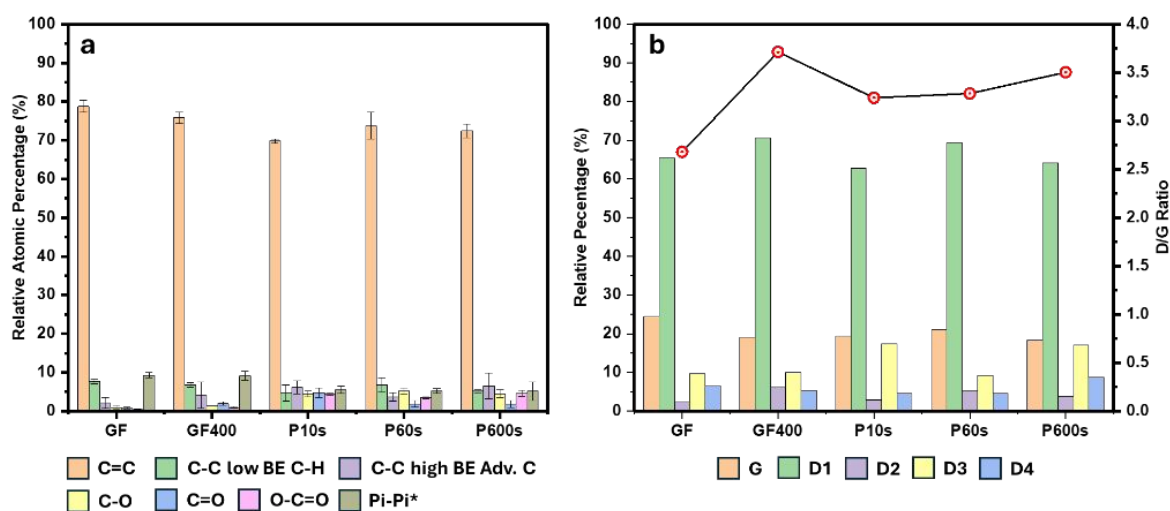


Figure 1: Bar charts showing, a) Relative percentages of the chemical functionalities deconvoluted from C1s XPS spectra of treated and untreated felts. b) Relative percentages of D and G bands deconvoluted from Raman spectra as well as D1/G ratio for treated and untreated felts.

Among the plasma treated materials, the shortest period of exposure (10 seconds, **P10s**) resulted in the largest oxygen population. It must be noted that although the oxygen content of **GF400** was found to be somewhat consistent across different measured samples, few super oxidised regions with oxygen contents between 11% and 21% and high population of carbonyl functionalities were observed (*Table S1* and *Fig. S3* in the SI document). The apparent inhomogeneity of the thermal treatment has been reported in previous thermal treatment studies and was caused by differences in graphitic edges or differences in the population of stable carbon oxides between samples of the same batch. Overall, these parameters impacted the wettability, capacitance and mass loss of the samples, however, the origin of these differences remained unclear.^{31, 32}

The distribution of oxygen-rich functional groups was analysed using the C1s and O1s high resolution spectra. The contributions arising from C(sp³), C(sp²), C-O associated with phenolic, ether or epoxy chemical shifts, C=O associated with quinone chemical shifts and O-C=O associated with carboxylate or lactone chemical shifts were used to deconvolute the C1s spectrum. The oxygen atomic percentage of the region associated with the high-resolution oxygen spectrum was used as criteria to adjust the quantities of the chemical shifts related to oxygen-rich functional groups in the C1s spectrum. Once a satisfactory fitting of the C1s region was obtained, the O1s spectrum was deconvoluted into C-O and C=O contributions considering the distribution of the different oxygen-rich functionalities found in the C1s spectrum. The feedback between the C1s and O1s was used as a way of confirming the



validity of the deconvolution models. A breakdown of the C1s spectrum deconvolution for all materials is shown in *Fig. 1a* and *Table S1* in the SI document.

The surface of the pristine **GF** consisted of C-O, C=O and O-C=O functional groups ($0.93\% \pm 0.48\%$, $0.76\% \pm 0.23\%$ and $0.45\% \pm 0.12\%$ respectively). On the other hand, **GF400**, exhibited twice as much overall oxygen content on the surface. The population of the C-O, C=O and O-C=O groups increased by 41%, 150% and 100%, respectively. On the other hand, the ROP treatment introduced between two and three times more oxygen on the surface of the GF compared to the thermal treatment. A comparison of the distribution of oxygen functionalities between **GF400** and the ROP-treated samples is displayed in *Table S1* from the SI document. The distribution of oxygen functionalities for **GF400** was C=O > C-O > O-C=O. On the other hand, **P10s** showed an even distribution of oxygen functionalities. For **P60s**, the distribution was C-O > O-C=O > C=O, whereas for **P600s** C-O and O-C=O dominated equally over C=O.

P10s exhibited slightly lower population of C-O functional groups compared to the other two longer plasma treatments. Populations of $4.38\% \pm 0.72\%$, $5.18\% \pm 0.77\%$ and $4.49\% \pm 0.93\%$ were determined for **P10s**, **P60s** and **P600s** respectively. However, all three values resulted within the same margin of error, which could suggest that either after the first few seconds, no new significant amounts of C-O groups are formed or that there is an interplay between the formation of new C-O functionalities with subsequent reactions to higher oxidations states and eventual decomposition as CO₂. This would render only few rich C-O regions in the fibres, with a larger presence of highly oxidated functional groups. C=O functionalities resulted more prominent in **P10s** with a population of $4.75\% \pm 1.22\%$ compared to $1.82\% \pm 0.84\%$ and $1.79\% \pm 0.93\%$ for **P60s** and **P600s**, respectively. These oxygen functional groups seemed to exhibit an initial increase to then experience a decrease and finally stabilize over a similar period. This trend suggests that the C=O groups were readily oxidised to O-C=O groups. Finally, for the O-C=O functionalities, similar concentrations were observed for **P10s** and **P600s**, whereas **P60s** exhibited the lowest value. The drop in the O-C=O atomic percentages around the first minute of plasma exposure with further recovery, suggest a dynamic degradation of the carboxylate functionalities by CO₂ evolution. In this scenario, the rate of degradation slows down over time, which gives opportunity to replenish the functionalities at extended periods of exposure.

Acidic oxygen groups such as phenolic and carboxylate have been reported to originate when carbon is thermally treated at temperatures close to its ignition point under oxygen atmosphere. Alternatively, neutral groups like quinone, ether, epoxy and ester are formed by chemisorption at mild temperatures.³² Neutral and acidic oxygen functionalities can decompose as CO₂ at lower temperatures.^{32, 33}

From these results, we can conclude that C-O functionalities develop up to a maximum concentration of around 4.7%. The concentration of C=O functionalities decreased after a few seconds of plasma treatment, whereas the population of O-C=O functionalities showed a fast development followed by a drop that then increases again with further exposure. Moreover, **P10s** exhibited the largest oxygen content (ca. 13.6%), while **P60s** and **P600s** showed slightly lower amounts (between 10.5% and 10.8%). These observations support the hypothesis that for the ROP treatment, there is a balance between CO₂ decomposition and replenishment of the oxygen functionalities over long exposure periods.

The surface of the carbon fibres was further investigated *via* Raman spectroscopy to analyse the degree of graphitisation and the nature of defects produced during the electrode treatments. The Raman spectra of all samples showed two characteristic peaks associated to graphitic materials between 1330 cm⁻¹ (D band) and 1590 cm⁻¹ (G band). The G band is associated to the in-plane vibration of graphitic C(sp²) lattices. Conversely, the D can be



decomposed into four contributions: D1 ($\sim 1330 \text{ cm}^{-1}$) associated to the total symmetric vibration of disordered graphitic lattice edges; D2 ($\sim 1620 \text{ cm}^{-1}$) associated to disordered graphitic superficial layer vibrations, D3 (1520 cm^{-1}) associated to amorphous $\text{C}(\text{sp}^2)$ domains, and D4 ($\sim 1200 \text{ cm}^{-1}$) associated to polyene structures present at defect sites in the periphery of graphitic domains or ionic impurities.^{28, 34} The analysis of the D1/G ratio is commonly used as a metric to determine the degree of defects on graphitic materials.

Several feasible sets of band contributions can be obtained by fitting the Raman spectrum employing different degrees of Gaussian and Lorentzian mixtures to define each Raman band. Allowing different ranges of full-width half maximum (FWHM) values will produce several potential suitable fittings. To avoid the bias associated with the choice of model, the pristine material was used to define the parameters of the fitting model which were then applied to the rest of the samples. The fitting parameters are reported in *Table S2* in the SI document.

A full breakdown of the relative percentages of the different bands as well as the D1/G ratio for the respective materials are shown in *Fig. 1b* and *Table S2* in the SI document. The **GF** sample exhibited D1/G ratio of 2.68. Ordered graphitic materials tend to exhibit larger G bands, which brings the $I_{\text{D}}/I_{\text{G}}$ to values closer to zero. The analysis suggests that the origin of the D1/G ratio in the pristine material could be related to the fibres surface being composed mainly of disordered graphitic domains, and amorphous $\text{C}(\text{sp}^2)$ carbon as opposed to ideal graphitic layers, in agreement with previous studies.³¹ The oxygen content of the pristine material obtained from XPS of around 2% would be more favourably bonded to carbon atoms located in the graphitic defective sites or the amorphous carbon domains, as oxygen functionalities are associated with these surface features.²⁸

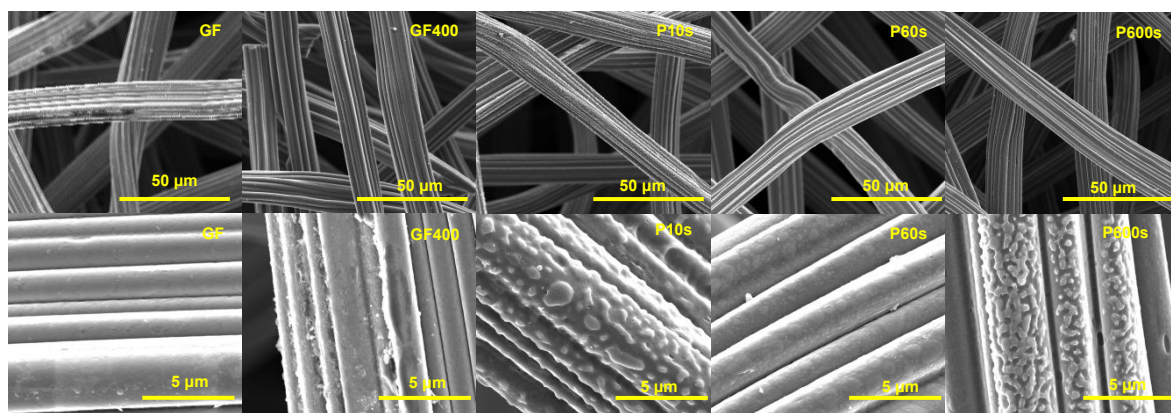


Figure 2: Scanning electron microscope images for the **GF**, **GF400**, **P10s**, **P60s** and **P600s** materials. p: x2600 magnification. Bottom: x20000 magnification.

GF400 exhibited the largest D1/G ratio of the studied materials (3.71). The most significant change in band contributions was the increase of the D1 and D2 bands and the decrease of the G band. The fitting contributions of the D3 and D4 bands were very similar to those from **GF**. This suggests that the thermal treatment leads to an increase in the number of disordered graphitic domains of the fibres, demonstrating that the surface modification mechanism of the thermal treatment predominantly induces the formation of defects and exposed edges with less significant impact on the amount of amorphous or polyene-like carbon.

P10s was characterised by a D1/G ratio of 3.24, while **P60s** and **P600s** exhibited D1/G ratios of 3.28 and 3.50, respectively. The increase in the D1/G ratio of **P10s** and **P600s** with respect



to **GF** was due to a significant increase in the D3 band, thus reducing the size of the G band. These results indicate that a shorter exposure to plasma generates various sites of superficial amorphous carbon. These features were in correlation with the XPS results which showed higher degree of carboxylate groups for these samples compared to **P60s**. On the other hand, the increase in the D1/G ratio of **P60s** was better explained by an increase of the D1 and D2 bands at the expense of the G band and a smaller contribution of the D3 band. Moreover, **P600s** showed the largest D4 band signal of the series, which in the case of **P10s** and **P60s** resulted very similar and smaller than **GF**. This suggests that plasma and thermal treatments follow different surface modification mechanisms. Raman analysis showed a development of graphitic defective sites and edges for **GF400** and to a lesser extend for **P60s** whereas for **P10s** and **P600s**, the formation of amorphous carbon domains was predominant.

The SEM micrographs of the treated felts showed that the samples exhibiting increase in amorphous carbon domains were characterised by rougher fibre surfaces. **P10s** exhibited a uniformly rough surface with large relief features of around 500 nm. **P600s** also exhibited similar features, but to a lesser extent, since the coverage in this case was not homogeneous and was limited to certain fibres. The inhomogeneity observed for **P600s** could be a consequence of the degradation of oxygen functionalities as CO₂, as discussed in the XPS section. This could etch the fibres, thus exposing fresh carbon. Conversely, **GF400** and **P60s** which were characterised by major increases in the graphitic edges and in plain defects exhibited smoother fibre surfaces. A potential explanation for the smoothing of **P60s** could be the same etching mechanism suggested for **P600s**. As discussed previously, a fast degradation rate over the first seconds of exposure could effectively remove the roughness. However, as the degradation rate slows down, it could give place to a balance between the formation of new oxygen functionalities and their degradation. Therefore, at longer periods of exposure, the fibres could recover some of the surface features observed for **P10s**.

Single-electrolyte cell characterisation.

The electrochemically active surface area (ECSA) of the electrodes were obtained via electrochemical double layer capacitance (EDLC) measurements in a single-electrolyte cell configuration using 2 M H₂SO₄. The EDLC is dependent on the quantity and mobility of the electrode charge carriers, which are associated to the defects on the graphitic surface.^{28, 31} The plasma treated felts displayed larger ECSA values compared to **GF**, with **P10s** and **P600s** reporting the largest difference, being ca. 2 times that of **GF**. However, **GF400** exhibited the largest ECSA of all samples, which is ca. 26 times that of **GF** and more than 12 times that of **P10s**. In principle, this result is consistent with the Raman analysis, which showed greater D1/G ratio for treated felts compared to **GF**, as it is expected that the graphitic defective sites and edges have larger EDLC than graphitic basal planes. The differences in EDLC and ECSA values between **GF400** and the ROP samples suggests that these may be related to the concomitant increase of graphitic defects observed by Raman spectroscopy.

The EDLC experiments also confirmed that the mechanism of surface modification by ROP treatment is inherently different from the thermal treatment, as the introduction of oxygen functionalities was not accompanied by a proportional increase in ECSA as observed for the thermal treatment. This was supported by the BET analysis which produced similarly increased specific physical surface areas for the ROP and thermal treated electrodes over the untreated one (*Table 1*). However, a closer look at the pore size distribution of these materials (*Fig. S17*) revealed that the **GF400** possesses a fraction of micropores (< 1 nm) not present in the other materials. During electrochemical measurements, access to these sites could serve as explanation for the order of magnitude increase in ECSA for **GF400**.



Overall, the general increase in specific surface area as shown in the BET data justifies the increase in ECSA observed for the treated materials. Notable however is how much lower the ECSAs are in comparison to these specific surface areas. This suggests that not all physical electrode surface area is available/accessible for electrochemical species to react. In this regard, surface area measurements obtained under electrochemical reaction conditions are more representative of the electrode availability during real cell operation conditions.³⁵

Table 1: EDLC and permeability extracted from pressure drop measurements.

Sample	EDLC ($\mu\text{F mg}^{-1}$)	ECSA ($\text{m}^2 \text{g}^{-1}$)	BET ($\text{m}^2 \text{g}^{-1}$)	Permeability $\times 10^{-11}$ (m^2)
Pristine	13.55	0.060	1.63	-
GF400	376.88	1.639	6.81	2.55
P10s	29.94	0.131	5.87	2.28
P60s	18.69	0.082	4.51	2.33
P600s	29.72	0.129	2.31	2.33

Pressure drop experiments were carried out to assess the pumping energy losses through the electrochemical cell for all electrodes. From these datasets, permeability was extracted using the Darcy-Forchheimer equation.²⁵ The permeabilities of the ROP electrodes all fell within ca. 2% difference of each other and ca. 12% less than **GF400** (Figs S24-S26). These results agree with the pore size distribution of the electrodes (Fig. S17). All ROP electrodes have similar pore size distributions and thus electrolyte flow paths are expected to be similar as reflected by their permeabilities. The fact that **GF400** displayed similar permeability to the ROP electrodes (only >12%), suggests that the primary flow paths are similar in both types of electrodes. In other words, the micropores may play little to no role in bulk electrolyte distribution though the electrode.

The performance of the thermal treated and ROP treated electrodes was analysed in a flow battery set up in single-electrolyte configuration. The electrolyte of choice was $\text{FeCl}_2/\text{FeCl}_3$ (0.25 M each for a total of 0.5 M iron) in 2M HCl, which is equivalent to a 50% state of charge (SoC). In single-electrolyte configuration, the electrolyte passes through both cathode and anode, carrying out the opposite electrochemical reaction on either side thus ensuring the battery operation proceeds always at a fixed SoC. This configuration ensures that the cell operates at steady-state conditions, which is an important requirement to obtain reliable impedance data. Moreover, this also ensures that there is no electrolyte crossover or self-discharge effects.^{24, 25} Polarisation and impedance data were acquired at four different flow rates across the whole range of our peristaltic pumps (between 15 and 110 mL min^{-1}).



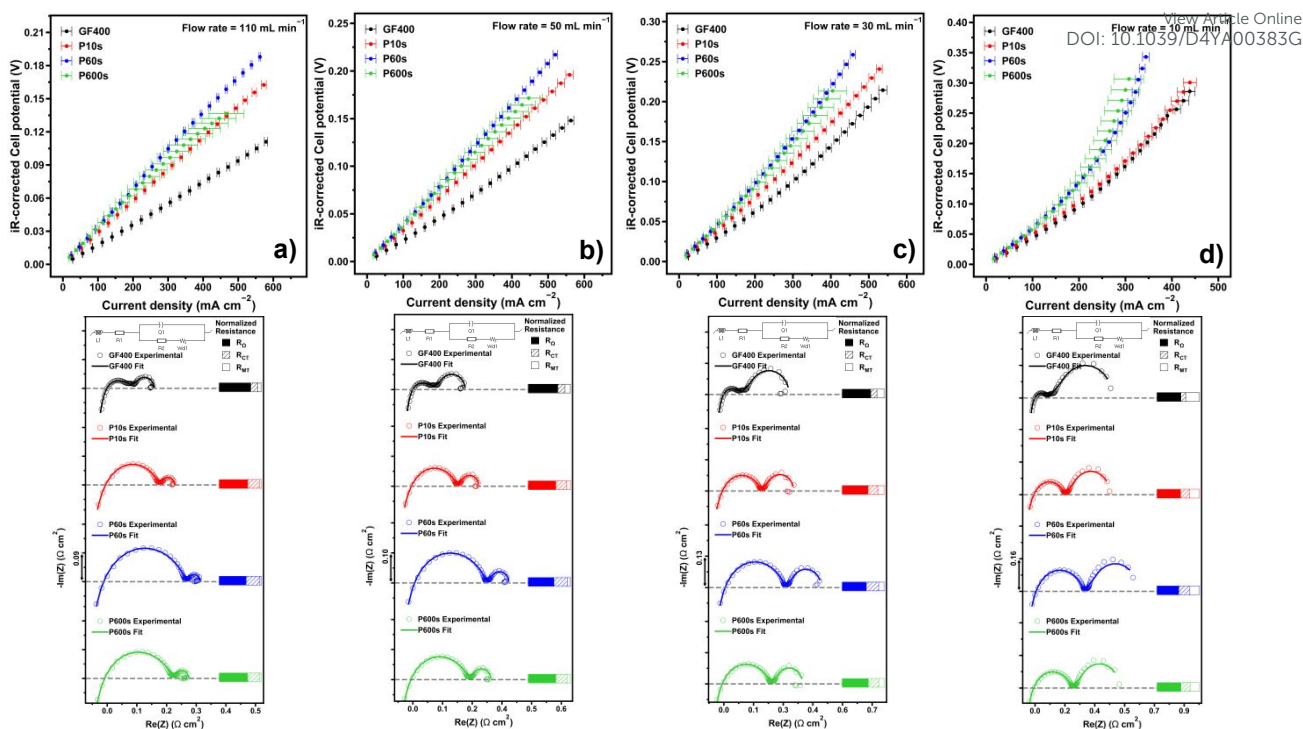


Figure 3: Single-electrolyte cell results. Top: polarisation data. Bottom: impedance data.

The purpose of using iron for this test is to employ a redox couple exhibiting well defined one-electron redox processes to simplify the deconvolution of the electrochemical impedance data into clear ohmic, charge-transfer and mass-transport contributions. The Nyquist plots of the single-electrolyte cells were characterised by two arcs, corresponding to high and low frequency impedance associated with the charge transfer and mass transport impedance respectively. The last few data points from the low frequency arc described a reduction in the magnitude of the real impedance. This was not the expected behaviour for the mass-transport impedance domain, and as such, the Warburg short circuit element employed to fit this segment was not able to model these data points. This anomalous behaviour is associated with the sluggish diffusion of ions through the fibrous carbon electrodes.

The ohmic resistance was obtained from the intercept of the impedance spectrum and the real impedance axis. The corresponding ohmic resistances were then subtracted from all Nyquist plots to normalise the onset of the impedance spectrum to simplify comparisons between samples. The ohmic resistance corresponds to the internal resistance of the cell, and since the same electrochemical setup was used to characterise all electrodes, the differences in this parameter were attributed to the conductivity differences of the electrodes. It was expected that the electrodes exhibiting higher degrees of oxygen coverage would be characterised by higher internal resistances. **GF400** exhibited 8% less internal resistance than **P10s**, 6% less than **P60s**, and 9% less resistance than **P600s**.

Limiting current densities were observed for the set of electrodes at low electrolyte velocity (*Fig. 3c-d*), and is indicative of a lack of readily available active reactant species.³⁶ With increasing electrolyte velocity, faster replenishment of active reactant species is enabled, diminishing this limitation and enhancing limiting current density.²⁵ This was observed as the polarisation plots became more linear with increasing flow rates for all electrodes. Not surprisingly, the mass transfer resistance of the cells also decreased with the increase of electrolyte flow rate, as the mass transfer resistance is associated with overpotential due the



limitations of supplying electroactive reactants to the active sites of the electrode surface and the diffusion coefficient of the active species which is constant in this case.^{37, 38} The charge transfer resistance contribution to the cell polarisation was also assessed. Charge-transfer resistance is associated with the kinetics of the iron redox process over the graphitic fibres surface, i.e. the kinetic overpotential. The charge transfer resistance contribution was observed to remain relatively consistent regardless of the flow rate for all electrodes.

When comparing polarisation plots of all electrodes clear trends were observed. The increase on the flow rate resulted in more notable differences in performance among the studied carbon electrodes. The general trend in performances across electrodes follow the order **GF400** > **P10s** > **P600s** > **P60s** (between flow rates 30ml min⁻¹ and 110ml min⁻¹). The opposite trend is observed when the averaged charge-transfer resistances across flow rates are taken. A closer look at the mass transfer resistance reveals a more complex relationship, with the only clear trend being **GF400** > **P10s**, **P60s** and **P600s**. In fact, all plasma treated electrodes exhibit ca. 35% less mass transfer resistance than **GF400**. Mass transfer is linked to diffusion coefficients, flow rates, but also intrinsic reaction kinetic parameters. The higher O content in ROP samples may be responsible for higher diffusivity of ions and potential higher intrinsic reaction kinetics that can translate into lower mass transport resistance. If we consider that as the flow rate increases, we approach infinitely fast mass transfer, then charge transfer resistance becomes the determining factor to limiting current density. As such, it makes sense for the polarisation performance to trend inversely to charge transfer resistance.

At lower flow rates, mass transfer resistance dominates, and therefore, due to its smaller mass-transport resistance, **P10s**, is able to overcome the larger ECSA and superior charge transfer capabilities of **GF400** (**GF400** resulted in 43%, 59% and 50% smaller charge transfer resistance than **P10s**, **P60s** and **P600s**), thus leading to comparable performance. This also highlights another observation of **GF400**, that despite having a magnitude size increase in ECSA, this does not translate into a more superior activity at all flow rates. Previous studies in the literature have demonstrated this limitation, attributing it to a limited accessibility to the electrode micropores by the reactive species.⁴ This idea was explored earlier when discussing the permeabilities of the electrode, which points to all the electrodes having the same general electrolyte flow trajectory. This was an expected feature, as the treatments were intended to modify the graphitic felts fibres surface and not the mesostructure of the materials. This finding is relevant because the common operation flow rates for real life flow battery applications lies between 10 and 30 ml min⁻¹.

Interestingly, the magnitude of the charge transfer resistance followed the order **P10s** < **P600s** < **P60s**, which was the same trend observed for the ECSA of the electrodes. As mentioned before, although this trend also coincides with the amount of carboxylate functional groups and the prevalence of amorphous carbon domains, the origin of the differences in the charge transfer resistance between samples are most probably associated with the differences in ECSA. Otherwise, the ROP felts should have exhibited inferior charge transfer resistances than **GF400** by virtue of their superior oxygen loading.

Conclusions

The surface of commercial GF electrodes was modified by a ROP using three different periods of exposure (10 s, 60s and 600 s) and their surface properties were compared to a common thermally treated felt. The XPS analysis of the samples indicated that all ROP-treated samples exhibited between two and three times larger superficial oxygen populations than the thermally treated sample. The C-O oxygen functionalities were found to remain constant among the three treatments whereas C=O groups were found more prominent for **P10s** and in similar quantities for **P60s** and **P600s**. Conversely, a larger amount of O-C=O functionalities were



found for **P10s** and **P600s** compared to **P60s**. The analysis of the Raman spectra of the samples showed that the pristine material exhibited the smallest D1/G ratio whereas **GF400** exhibited the highest D1/G ratio. Among the ROP treated materials, the D1/G ratio increased in correlation with the exposure period. The deconvolution of the D band showed that the thermal treatment favoured the increase of D1 and D2 bands associated with the vibrations of defective graphitic domains. For **P10s**, the major contribution to explain the D1/G ratio came from an increase of the D3 band, associated with amorphous carbon domains. **P60s** exhibited major increases in the D1 and D2 bands, and minor increases in the D3 band. **P600s** also exhibited larger contributions from the D3, although an increase of the D4 was also observed. The SEM micrographs of the samples showed rough features covering the majority of the **P10s** fibres and to a lesser extent in **P600s**. Conversely **GF400** and **P60s** were characterised by smoother fibres and absence of distinctive features.

EDLC and BET experiments showed all treated materials were characterised by larger surface areas than the pristine material. However, for all samples the ECSA resulted significantly lower than the BET area, illustrating the low accessibility of the electrode surface for electrochemical reactions. **GF400** exhibited the largest physical surface area and ECSA among all the treated samples despite not being the sample with the largest number of oxygen-functionalities. Moreover, **GF400** showed a distinctive fraction of microporosity, which was not found in any of the ROP treatments. The permeability of all treated materials resulted in **GF400** resulting in 12% higher permeability than the ROP treated materials which showed similar values regardless of the exposure period.

The single-electrolyte polarisation and impedance experiments revealed that **GF400** exhibited between 43-59% lower charge-transfer resistance than the ROP treated-samples. This indicated that the kinetic overpotential improvements were driven by the ECSA not by the amount of superficial oxygen functionalities. The magnitude of the charge-transfer resistance among the ROP samples followed the same trend as the ECSA, further supporting that the kinetic overpotential improvements were due to increases in the ECSA. The mass-transport resistance of all ROP treated materials resulted ca. 35% lower than **GF400**. At fast flow rates, when the kinetic overpotential is the most important contribution to the electrode polarisation, **GF400** resulted in the best performing sample. However, at slower flow rates, when the mass transport overpotential becomes the dominant contribution to the polarisation, the performance of **GF400** and **P10s** became comparable. Overall, this report provides an insight on the effects of oxygen-enriching surface treatments for graphite felt electrodes in terms of surface chemistry, defects, ECSA, porosity and their correlation with flow cell performance.

Author contributions:

L. M. M. H., C. M., and M. T.: Characterisation of the materials, data analysis, manuscript drafting. J. O. P., and J. R. S.: preparation of the materials. A. B. J. S.: Conceptualisation of the project, writing-review & editing. A. B. J. S.: Funding acquisition.

Conflicts of interest

The authors declare that there are no conflicts of interest.

Acknowledgements

A. B. J. S. acknowledges the UK Research and Innovation for Future Leaders Fellowship no. MR/T041412/1.

References.



1. K. E. Rodby, T. J. Carney, Y. A. Gandomi, J. L. Barton, R. M. Darling and F. R. Brushett, *J. Power Sources*, 2020, **460**, 227958-227969. View Article Online
DOI: 10.1059/D4TA00383G
2. A. Fornier-Cuenca and F. R. Brushett, *Current Opinion in Electrochemistry*, 2019, **18**, 113-122.
3. J. P. Tafoya, M. Thielke, G. Tian, R. Jervis and A. B. Sobrido, *Current Opinion in Chemical Engineering*, 2022, **38**, 100876-100885.
4. K. V. Greco, J. K. Bonesteel, N. Chanut, C. T.-C. Wan, Y.-M. Chiang and F. R. Brushett, *ACS Applied Energy Materials*, 2021, **4**, 13516-13527.
5. B. Sun and M. Skyllas-Kazacos, *Electrochim. Acta*, 1992, **37**, 1253-1260.
6. S. J. Yoon, S. Kim, H. Kim, D. K. Kim, S. So, Y. T. Hong and R. Hempelmann, *Carbon*, 2020, **166**, 131-137.
7. R. Wang, Y. Li, Y. Wang and Z. Fang, *Applied Energy*, 2020, **261**, 114369.
8. K. J. Kim, H. S. Lee, J. Kim, M.-S. Park, J. H. Kim, Y.-J. Kim and M. Skyllas-Kazacos, *ChemSusChem*, 2016, **9**, 1329-1338.
9. K. Amini, J. Gostick and M. D. Pritzker, *Adv. Funct. Mater.*, 2020, **30**, 1910564.
10. Y. Lv, C. Han, Y. Zhu, T. Zhang, S. Yao, Z. He, L. Dai and L. Wang, *Journal of Materials Science & Technology*, 2021, **75**, 96-109.
11. Y. Zhang, L. Liu, J. Zi, Z. Wu and X. Qiu, *Applied Energy*, 2017, **204**, 373-381.
12. M. W. Thielke, G. Tian and A. Jorge Sobrido, *Journal of Physics: Materials*, 2022, **5**, 024004.
13. A. Kaur, K. I. Jeon, S. S. Kim and J. W. Lim, *Compos. Struct.*, 2022, **290**, 115546-115548.
14. K. V. Greco, A. Fornier-Cuenca, A. Mularczyk, J. Eller and F. R. Brushett, *Applied Materials & Interfaces*, 2018, **10**, 44430-44442.
15. A. M. Pezeshki, J. T. Clement, G. M. Veith, T. A. Zawodzinski and M. M. Mench, *J. Power Sources*, 2015, **294**, 333-338.
16. P. C. Ghimire, R. Schweiss, G. G. Scherer, T. M. Lim, N. Wai, A. Bhattarai and Q. Yan, *Carbon*, 2019, **155**, 176-185.
17. L. M. Murillo-Herrera, E. S. Aguilar, M. W. Thielke and A. Jorge Sobrido, *Chemistry – An Asian Journal*, 2023, **18**.
18. L. Yue, W. Li, F. Sun, L. Zhao and L. Zing, *Carbon*, 2010, **48**, 3079-3090.
19. B. Sun and M. Skyllas-Kazacos, *Electrochim. Acta*, 1992, **37**, 2459-2465.
20. D. Dixon, D. J. Babu, J. Langner, M. Bruns, L. Pfaffmann, A. Bhaskar, J. J. Schneider, F. Scheiba and H. Ehrenberg, *J. Power Sources*, 2016, **332**, 240-248.
21. C.-H. Lin, Y.-D. Zhuang, D.-G. Tsai, H.-J. Wei and T.-Y. Liu, *Polymers*, 2020, **12**, 1372.
22. T. Jirabovornwisut, B. Singh, A. Chutimasakul, J.-H. Chang, J.-Z. Chen, A. Arpornwichanop and Y.-S. Chen, *Materials*, 2021, **14**, 3487.
23. M. Alcaire, F. J. Aparicio, J. Obrero, C. López-Santos, F. J. Garcia-Garcia, J. R. Sánchez-Valencia, F. Frutos, K. Ostrikov, A. Borrás and A. Barranco, *Adv. Funct. Mater.*, 2019, **29**, 1903535.
24. R. M. Darling and M. L. Perry, *ECS Transactions*, 2013, **53**, 31-38.
25. C. T.-C. Wan, R. R. Jacquemond, Y.-M. Chiang, A. Fornier-Cuenca and F. R. Brushett, *Energy Technology*, 2023, **11**, 2300137.
26. R. R. Jacquemond, C. T.-C. Wan, Y.-M. Chiang, Z. Borneman, F. R. Brushett, K. Nijmeijer and A. Fornier-Cuenca, *Cell Reports Physical Science*, 2022, **3**, 100943.
27. J. D. Milshtein, K. M. Tenny, J. L. Barton, J. Drake, R. M. Darling and F. R. Brushett, *J. Electrochem. Soc.*, 2017, **164**, E3265-E3275.
28. J. Langner, M. Bruns, D. Dixon, A. Nefedov, C. Wöll, F. Scheiba, H. Ehrenberg, C. Roth and J. Melke, *J. Power Sources*, 2016, **321**, 210-218.
29. J. Lee, J. T. Muya, H. Chung and J. Chang, *ACS Applied Materials & Interfaces*, 2019, **11**, 42066-42077.
30. D. Kil, H. J. Lee, S. Park, S. Kim and H. Kim, *Journal of Electrochemical Society*, 2017, **164**, A3011-A3017.
31. T. J. Rabbow, M. Trampert, P. Pokorny, P. Binder and A. H. Whitehead, *Electrochim. Acta*, 2015, **173**, 17-23.



32. T. J. Rabbow, M. Trampert, P. Pokorny, P. Binder and A. J. P. White, *Electrochim. Acta*, 2015, **173**, 24-30. View Article Online
DOI: 10.1039/D4TA00383G
33. C. A. Frysz, X. Shui and D. D. L. Chung, *Carbon*, 1994, **32**, 1499-1505.
34. M. W. Thielke, S. Lopez Guzman, J. P. Victoria Tafoya, E. García Tamayo, C. I. Castro Herazo, O. Hosseinaei and A. Jorge Sobrido, *Frontiers in Materials*, 2022, **9**, 1-10.
35. T. J. Rabbow and A. H. Whitehead, *Carbon*, 2016, **111**, 782-788.
36. D. Aaron, Z. Tang, A. B. Papandrew and T. A. Zawodzinski, *J. Appl. Electrochem.*, 2011, **41**, 1175-1182.
37. A. Forner-Cuenca, E. E. Penn, A. M. Oliveira and F. R. Brushett, *J. Electrochem. Soc.*, 2019, **166**, A2230-A2241.
38. M. Van Der Heijden, M. Kroese, Z. Borneman and A. Forner-Cuenca, *Advanced Materials Technologies*, 2023, **8**, 2300611.



Data availability statement

View Article Online
DOI: 10.1039/D4YA00383G

The data sets generated in this work are available upon request to the first and corresponding author.

